

Combined DFT, AFM, and Cryogenic Transport Study of a Niobium Thin Film

Giacomo Bertelli †

Sofia Grandi *

Federico Guglielmi *

Federico Muscarà ♦

Alberto Polato ♦

Eva Ricci †

Francesco Zanasi ♦

*: ABINIT †: AFM analysis ♦: Resistivity

I. INTRODUCTION

The superconducting properties of niobium have been studied for several decades, primarily due to its relatively high critical temperature. Recently, however, niobium has gained renewed attention because of its unique superconducting characteristics and its potential applications in various fields. High purity niobium is the material of choice for fabricating superconducting radio-frequency cavities for particle accelerators [1], [2]; it is highly employed to engineer superconductive quantum sensors such as SNSPDs, able to detect single particles [3], [4], or SQUIDs, sensitive to magnetic fields in the order of the flux quantum (10^{-15} T) [5], [6]; it is widely utilized in the fabrication of Josephson junctions qubits for quantum computing [7], [8]. This paper presents a comprehensive study of niobium thin films, focusing on three key numerical and experimental techniques: Density Functional Theory (DFT) calculations, Atomic Force Microscopy (AFM) measurements, and cryogenic resistivity measurements.

AFM measurements yield valuable insights into the surface morphology and topography of niobium thin films, enabling the characterization of film quality and the identification of structural properties such as granularity and film thickness, which may significantly influence their electrical properties.

Cryogenic resistivity measurements allow for the investigation of superconducting behavior, including the determination of critical temperatures and magnetic fields, offering a deeper understanding of the material's performance under varying conditions. Complementing these experimental approaches, DFT and DFPT calculations provide a theoretical framework for predicting electronic and superconductive properties.

By integrating these methodologies, this study aims to clarify the relationship between the structural, electronic, and superconducting properties of niobium thin films, justified by comparison with both theoretical and literature results.

In Section II we present the theoretical predictions from Density Functional (Perturbation) Theory, implemented by means of ABINIT simulations of niobium electronic and phonon properties. In Section III we report the results obtained from the structural characterization of our niobium sample thickness and texture performed by AFM acquisitions. Finally, Section IV details the experimental procedure behind cryogenic resistivity measurements, from which we extract

experimental data to calculate electronic and superconductive properties of the sample.

II. ABINIT SIMULATION

ABINIT simulations implement numerical resolution of the Hamiltonians based on Density Functional Theory (DFT). The core of ground-state DFT revolves around the solution of Kohn-Sham eigenvalue problem (1) which basically maps the atomic many-electron Hamiltonian into the single electron Hamiltonian \hat{H}^{KS} , from which one can extract all the electronic properties starting from the atomic ground-state density.

$$\hat{H}^{\text{KS}} \phi_{nk}^{\text{KS}} = \varepsilon_{nk}^{\text{KS}} \phi_{nk}^{\text{KS}} \quad (1)$$

Specifically, we performed simulations to evaluate niobium's ground-state, electronic and phononic properties and electron-phonon interaction. To ensure the correctness of results, we must perform a preliminary convergence study with respect to the following DFT parameters:

- The cutoff energy E_{cut} (ecut) determining the size of the set of plane waves $\{\varphi_G(\mathbf{k}, \mathbf{r}) = e^{i(\mathbf{k} + \mathbf{G}) \cdot \mathbf{r}}\}$ used for series-expansion of the Kohn-Sham eigenfunctions as

$$\phi_{nk}^{\text{KS}}(\mathbf{r}) = \sum_{\mathbf{G}} c_{nk} \varphi_{\mathbf{G}}(\mathbf{k}, \mathbf{r}) \quad (2)$$

All the plane waves whose kinetic energy $\hbar^2 |\mathbf{k} + \mathbf{G}|^2 / 2m_e$ exceeds E_{cut} are excluded from the expansion. Bigger sets lead to higher accuracy at the cost of longer computation times;

- The number of k -points ($ngkpt$) in the first Brillouin zone where the eigenvalue problem is evaluated after being translated from (1) to the matrix equation in (3):

$$\mathbf{H}^{\text{KS}}(\mathbf{k}) \mathbf{c}_{nk} = \varepsilon_{nk} \mathbf{c}_{nk} \quad (3)$$

Again, higher values correspond to a denser mesh resulting in a more precise computation of electronic properties. Here again, there is a tradeoff between k -grid size and the computation times.

- The smearing temperature σ ($tsmear$) is a parameter introduced to counteract numeric instability when calculating electronic properties around the Fermi energy, due to the sudden step of the Fermi distribution at 0K. A smearing function $\delta(\varepsilon) = \tilde{\delta}(\varepsilon/\sigma)/\sigma$ is chosen to broaden the distribution by a certain amount, parametrized by σ . We adopted

the Marzari *cold smearing* function $\tilde{\delta}(\varepsilon)$ in (4) with $a = -0.5634$ (minimization of the bump):

$$\tilde{\delta}(\varepsilon) = (1.5 + \varepsilon(-1.5a + \varepsilon(-1 + a\varepsilon))) e^{-\varepsilon^2/\sqrt{\pi}} \quad (4)$$

Experimentally, it has been found that the convergence with respect to E_{cut} is reasonably independent from the k -grid and smearing temperature, which instead are heavily inter-dependent. In order to assess convergence, in the following we will consider the total energy E_{tot} of the crystal as it settles to a stable, converged value.

Fig. 1 reports the convergence study of E_{tot} with respect to E_{cut} , keeping $\sigma = 1 \mu\text{Ha}$ and using a $28 \times 28 \times 28$ Monkhorst-Pack k -grid. We decided to choose $E_{\text{cut}} = 42 \text{ Ha}$ for all successive computations, as it gives an error on E_{tot} of less than $3 \mu\text{Ha}$ with respect to a fully converged value.

Fig. 2 shows the convergence of E_{tot} with respect to Monkhorst-Pack grid size and smearing temperature. We highlight how increasing the k -grid size to big values still gives small oscillations of $\sim 20 \mu\text{Ha}$ in E_{tot} at low smearing temperatures. Taking as reference the point-by-point average of the four curves with largest k -grid (compensation for the oscillation), we opt for $\sigma = 9 \mu\text{Ha}$ and a $18 \times 18 \times 18$ k -grid, as this choice guarantees:

- A distance to the average curve of less than $30 \mu\text{Ha}$;
- An error of E_{tot} with respect to the projected value at $\sigma = 0$ of less than $100 \mu\text{Ha}$;
- A sufficiently big value of σ as not to slow down excessively the computations.

Before further computations, it is crucial to (numerically) relax the crystal. We performed this step by allowing ABINIT to conduct structural optimization, using the Broyden-Fletcher-Goldfarb-Shanno minimization, on the cell volume until a tolerance of $5 \cdot 10^{-5} \text{ Ha}/\text{Bohr}$ on the maximal absolute force is reached. Using this procedure, we obtained a lattice

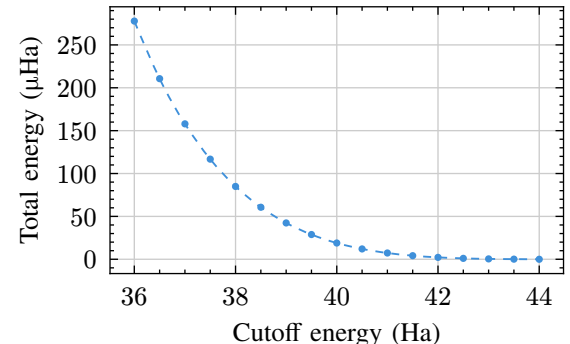


Fig. 1. Convergence curve of total energy (with an offset) with respect to the cutoff energy. A value of $E_{\text{cut}} = 42 \text{ Ha}$ guarantees an error on total energy less than $3 \mu\text{Ha}$ with respect to the converged value.

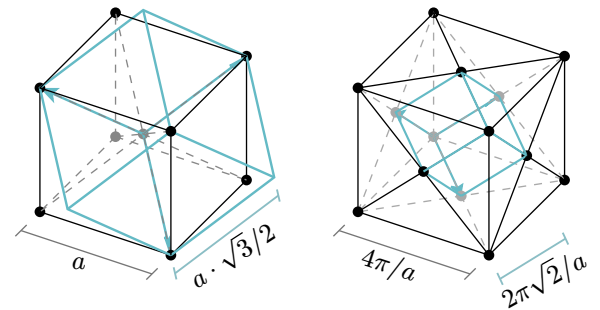


Fig. 3. Unit cell of Niobium crystal in both real space (BCC; left side) and reciprocal space (FCC; right side). Black lines represent the traditional cell, whereas the light blue ones represent the primitive cell. a is the lattice constant, which has been experimentally found to be 330.5 pm at 20°C [9].

constant $a_{\text{rlx}} = 331.271 \text{ pm}$, which differs from the experimental value of $a_{\text{exp}} = 330.05 \text{ pm}$ at 20°C [9] (used as first guess) by less than 0.4% . As a reference, the unit cell of Niobium is reported in Fig. 3.

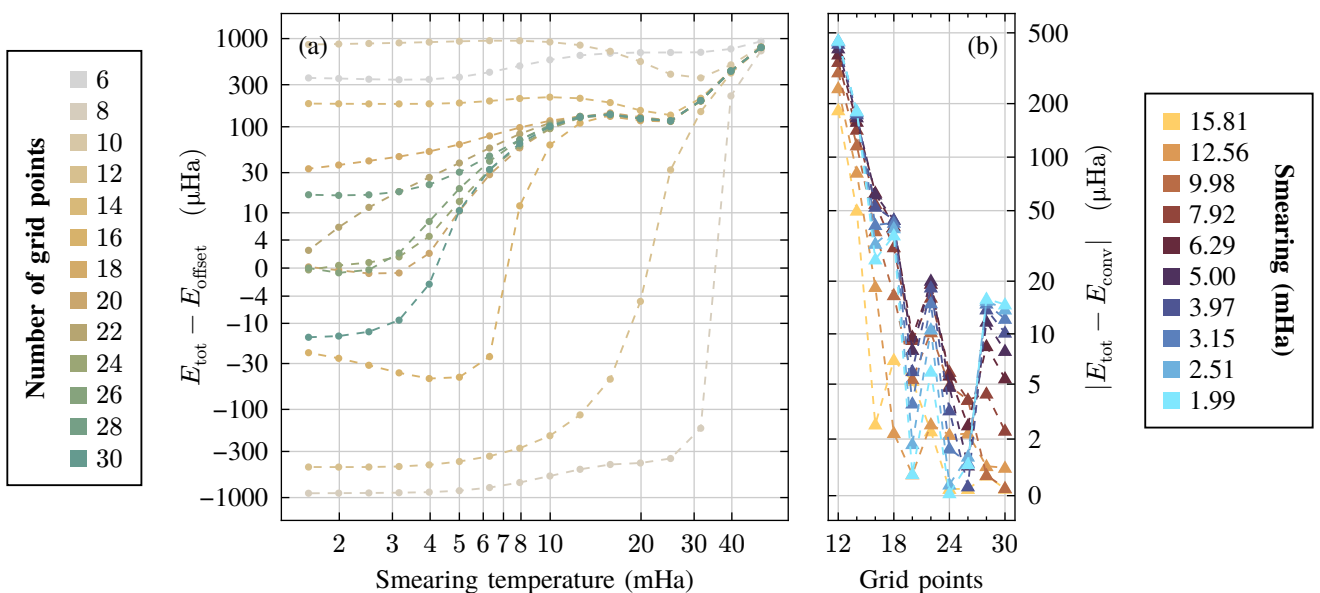


Fig. 2. Convergence of total energy with respect to the size of Monkhorst-Pack grid and smearing temperature. (a) The total energy (with an offset) is plotted (in *symlog* scale) against the smearing temperature (in *log* scale), for different sizes of the k -grid. (b) The absolute difference between the total energy and converged total energy E_{conv} (in *symlog* scale) against the k -grid size, for a subset of smearing temperatures. E_{conv} is approximated as the point-by-point average of the four curves on the left with the largest k -grid.

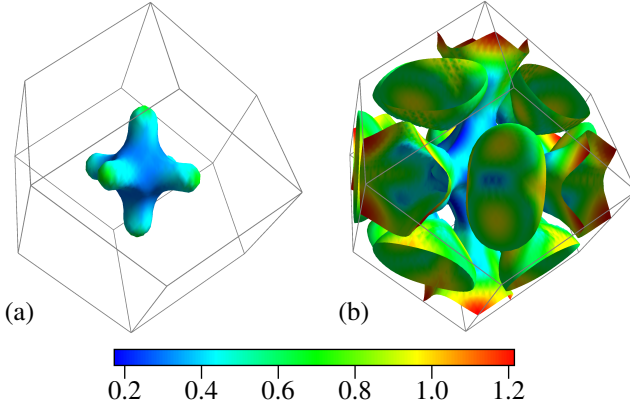


Fig. 4. Fermi surface of niobium, folded in the first Brillouin zone, lit from the occupied side, and colored based on the Fermi velocity (km/ms). (a) In the second zone, the Fermi surface is a closed structure with octahedron symmetry, centered at the Γ point. (b) In the third zone, the Fermi surface is composed of an open *jungle-gym* geometry (as first termed in [15]) and distorted ellipsoids centered at the N points.

A. Electronic properties

Using ABINIT we computed the bands around the Fermi energy, taking into account spin-orbit coupling. The results are reported in Fig. 5, and are in agreement with previous findings in literature [10], [11]. Moreover, the angular-momentum projected density of states was also computed to determine the orbital contributions (Fig. 7). As expected, the density of states around the Fermi energy is mainly dominated by d orbitals ($l = 2$), and its first derivative at E_F is negative, implying a hole-like conduction. We report the following relevant quantities derived from the density of states:

- $N_F := \text{DOS}(E_F) = 1.478 \text{ electrons/eV/cell}$
- Charge density $N_v = 5.008 \text{ electrons/cell}$
- Fermi energy $E_F = 5.893 \text{ eV}$, referenced from the bottom of conduction bands

Fig. 4 reports the obtained Fermi surface of niobium, folded in the first Brillouin zone, which is in agreement with previous findings in literature [12], [13], [14]. By averaging the square norm of the Fermi velocity on such surface over all the bands crossing E_F , we obtain $\sqrt{\langle v_F^2 \rangle} = 7.004 \cdot 10^5 \text{ m s}^{-1}$. Adopting an analogous procedure with the harmonic mean of the eigenvalues of the mass tensor leads us to the (conductivity) effective mass $\langle 1/m_{\text{eff}} \rangle^{-1} = -2.088 m_e$. We highlight the negative sign of such result: indeed the density of states has negative slope at the Fermi energy. Moreover this result is well compatible (in absolute value) with the range of values obtained experimentally through de Haas-van Alphen effect [12] (from $0.27m_e$ to $3.1m_e$, depending on direction).

For further details on the adopted procedure for the evaluation of $\langle v_F^2 \rangle$ and $\langle 1/m_{\text{eff}} \rangle$ and for details on their range of values in the Brillouin zones, please refer to Appendix A.

B. Phonon properties

Within the DFT framework, phonon properties are computed by means of Density Functional Perturbation Theory. The latter computes the linear response of the ground-state electron density with respect to the displacement of the nuclei from their equilibrium position (q -vectors). These computa-

tions are notably more time-consuming than the ones for the electronic ground state. Therefore some compromise must be done with respect to the size of k - and q -grids. We first decided to perform computations with a $6^{3 \times 3}$ q -grid. However we soon reckoned it being too small for a fully converged computation: phononic bands are partially shifted from the experimental measurement and the Eliashberg function peaks do not align to experimental data (both graph are reported for completeness in Appendix C). Hence, we decided to increase the size of the q -grid to $12^{3 \times 3}$ at the expense of a smaller k -grid ($12^{3 \times 3}$ instead of $18^{3 \times 3}$), leading to a computation time of c.a. 26 hours. All the following discussions refer to this latter configuration of grids. Table III instead reports some derived quantities for both grid configurations.

Fig. 6 reports the phononic bands and density of states. Although the calculation is not fully converged with respect to the grid, we highlight how the phononic bands are in reasonable agreement with the experimental dispersion relation measured in [16] by neutron scattering technique.

From the bands' data, we evaluate the speed of sound by performing a spherical average using Lebedev-Laikov grids on a small q -sphere. Using a q -radius of 0.1 Bohr^{-1} , we obtain an average speed of sound $v_s = (3.17 \pm 0.01) \text{ km s}^{-1}$, which is relatively close to the 20°C speed of sound in niobium of 3.48 km s^{-1} [17]. Table III also reports v_s for each phononic band.

From the phononic density of states, it is possible to derive an “equivalent” Debye temperature. We consider the low-energy part of the DOS and we fit a parabola against it; we then extend the latter until its integral is equal to 3 i.e. the integral of the phonon DOS. The procedure is detailed in Appendix B. In this way, we obtain $\Theta_D = 235.6 \text{ K}$, which is loosely close to the experimental values from literature of 276 K [18] and 275 K [19] (c.a. 14% error).

C. Electron-phonon coupling

The electron-phonon interaction is responsible for a wide range of material properties, including electrical resistivity and, most notably, superconductivity. The strength of this interaction is quantified by the electron-phonon matrix elements $g_{n,m}^\nu(\mathbf{k}, \mathbf{q})$ which represent the probability of an electron absorbing or emitting a phonon. The electron-phonon spectral (Eliashberg) function $\alpha^2 F(\omega)$ is a crucial quantity derived from these matrix elements, as it assesses the coupling strength between electrons and phonon modes. In particular, through DFPT we computed both the thermodynamic Eliashberg function:

$$\alpha_{\text{th}}^2 F(\omega) = \sum_{\mathbf{k}, \mathbf{q}, n, m, \nu} |g_{n,m}^\nu(\mathbf{k}, \mathbf{q})|^2 \delta(\varepsilon_{\mathbf{k}}^n) \delta(\varepsilon_{\mathbf{k}+\mathbf{q}}^m) \delta(\omega - \omega_q^\nu) \frac{1}{N_F}$$

and the transport Eliashberg function:

$$\alpha_{\text{tr}}^2 F(\omega) = \frac{1}{2N_F \langle v_F^2 \rangle} \sum_{\mathbf{k}, \mathbf{q}, n, m, \nu} [v_F(\mathbf{k}) - v_F(\mathbf{k} + \mathbf{q})]^2 |g_{n,m}^\nu(\mathbf{k}, \mathbf{q})|^2 \delta(\varepsilon_{\mathbf{k}}^n) \delta(\varepsilon_{\mathbf{k}+\mathbf{q}}^m) \delta(\omega - \omega_q^\nu)$$

Fig. 8 reports both functions, as well as the experimental (thermodynamic) spectral function $\alpha^2 F_{\text{PETS}}$ obtained via

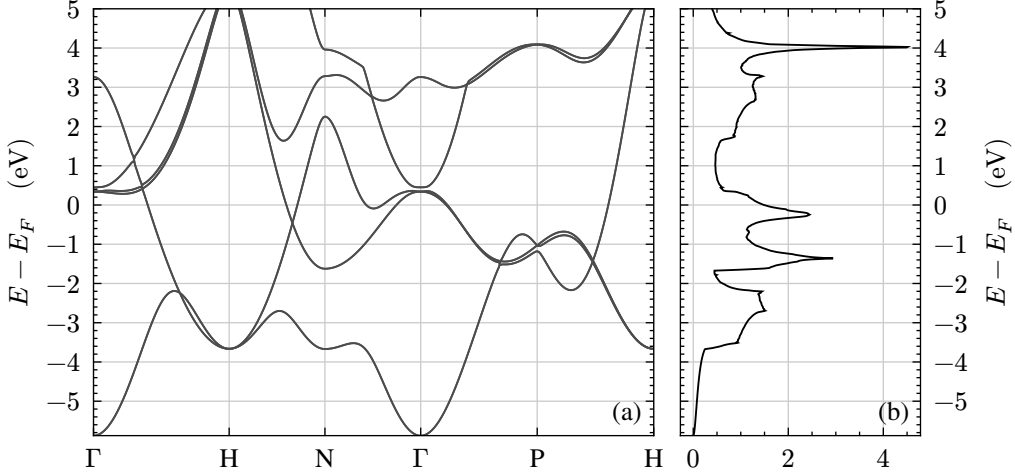


Fig. 5. Electronic states of niobium, around its Fermi energy, obtained using a $18 \times 18 \times 18$ Monkhorst-Pack k -grid. (a) Band structure; please note that each curve actually represents two degenerate one-electron bands. (b) Density of states – in electrons/eV/cell – colored based on the orbital contribution: s in blue, p in red, and d in gray. As expected, energy states around the Fermi energy are mostly due to d orbitals and the conduction is hole-like since the first derivative of the DOS is negative at E_F

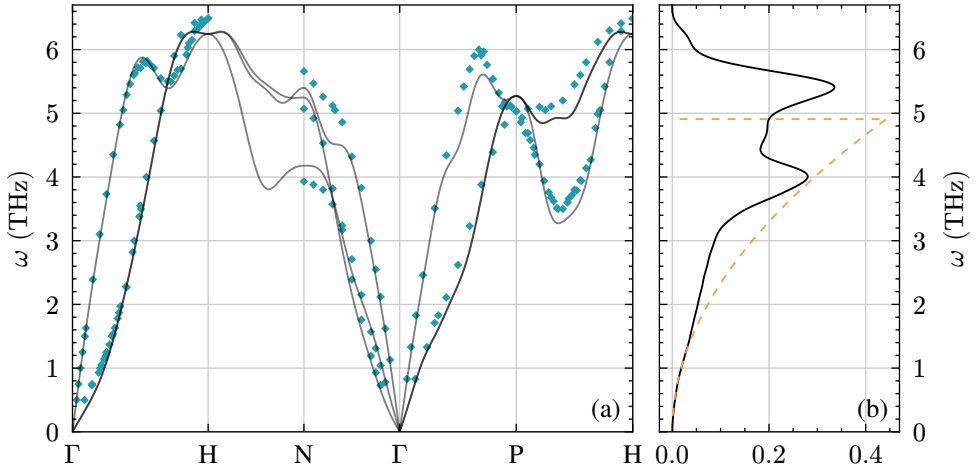


Fig. 6. Phononic states of niobium, obtained using 12×3 Monkhorst-Pack k - and q -grids. Although the curves are not fully converged with respect to the grids' size, they are in reasonable agreement with the experimentally measured dispersion [16] reported in cyan. (a) Band structure: curves are slightly transparent so that a darker color represent an overlap of two bands. (b) Solid black curve: density of states in states/meV; orange dashed curve: Debye model obtained by fitting initial parabolic trend ($\Theta_D = 235.6$ K).

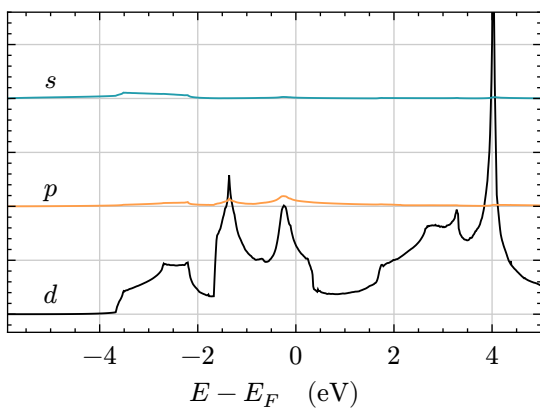


Fig. 7. Orbital-projected electronic density of states. Due to how this projection is implemented, the contribution numerically do not add up to the total density of states of Fig. 5;b. Therefore units are not reported on the y -axis. Each contribution is reported with the same scale, but different visual offset.

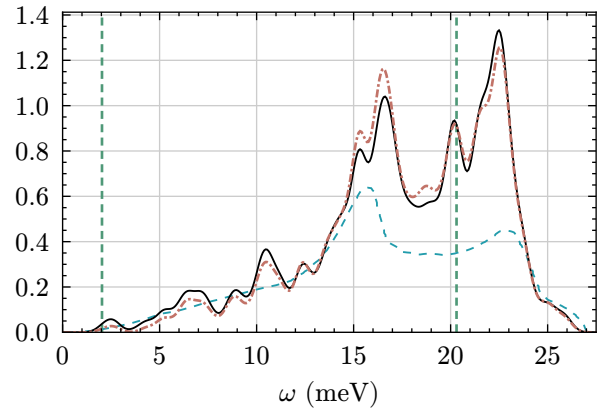


Fig. 8. Eliashberg spectral function as function of phonon frequency, obtained using a 12×3 k - and q -grid. The blue dashed line represent the experimental (thermodynamic) $\alpha^2 F_{\text{PETS}}$ obtained through proximity electron tunneling spectroscopy [20]. The solid black and dash-dotted curves red are respectively the thermodynamic and transport electron-phonon spectral functions $\alpha_{\text{th}}^2 F$ and $\alpha_{\text{tr}}^2 F$. The two green dashed vertical lines denote $\Theta_D/10$ and Θ_D .

proximity electron tunnelling spectroscopy [20]. Although the shape qualitatively follows previous computations in literature [21], [22], we highlight how our curve is less smooth: this fact is likely due to the q - and k -grids being too coarse for fully converged calculations.

Using the knowledge of the Eliashberg function(s), we derived two other key parameters: the electron-phonon coupling constant $\lambda_{\text{th}} = 1.350$, $\lambda_{\text{tr}} = 1.277$ – equation (5) – and the logarithmic average of the phonon frequencies $\omega_{\log}^{\text{th}} = 13.443 \text{ meV}$, $\omega_{\log}^{\text{tr}} = 14.665 \text{ meV}$ – equation (6). As expected $\lambda_{\text{th}} > \lambda_{\text{tr}}$ due to the impact of small-angle scattering.

$$\lambda = 2 \int_0^\infty d\omega \alpha^2 F(\omega) / \omega \quad (5)$$

$$\omega_{\log} = \exp \int_0^\infty d\omega \alpha^2 F(\omega) \frac{2 \log \omega}{\lambda \omega} \quad (6)$$

Employing the Allen-Dynes form of the semi-empirical McMillan formula (7) and the empirical value $\mu^* = 0.24$ for the Morel-Anderson pseudo-potential [12], we finally estimate the critical temperature to be $T_c = 8.844 \text{ K}$. Although the results are not fully converged, we highlight how this value of critical temperature is close to the experimental value of the present — $(7.426 \pm 0.040) \text{ K}$ at 0 T for a 62 nm film — and past works — $T_c \approx 9.3 \text{ K}$ [23], [24] for bulk, high-purity niobium.

$$T_c = \frac{\omega_{\log}^{\text{th}}}{1.2} \exp \left[-\frac{1.04(1 + \lambda_{\text{th}})}{\lambda_{\text{th}} - \mu^*(1 + 0.62\lambda_{\text{th}})} \right] \quad (7)$$

III. AFM ACQUISITION

This section illustrates the analysis of the data acquired measuring a thin film of niobium with the same properties of the one used in Section IV¹. All the measurements were performed using a *Bruker Innova* Atomic Force Microscope in *tapping mode*, with drive frequency of c.a. 282.26 kHz and scanning rates between $0.5 \text{ } \mu\text{m s}^{-1}$ and $20 \text{ } \mu\text{m s}^{-1}$, depending

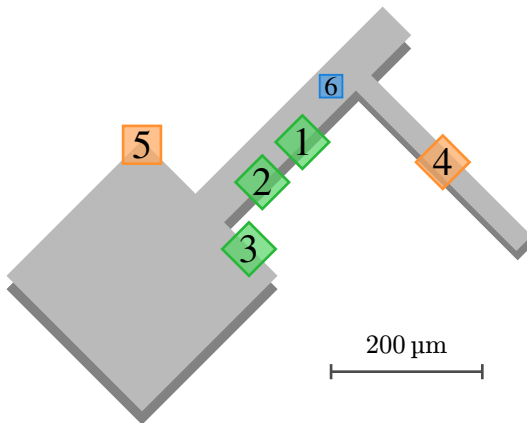


Fig. 9. Schematic representation of the sample (gray) and the approximate location of the measurement regions.

¹The two samples have been obtained from the same wafer and are thus assumed to have the same properties. Due to instrumentation constraints, it was not possible to inspect under the AFM the sample used in the low-temperature measurements.

on the region and image size. Moreover, both topological and phase data were collected. Different regions of the film were sampled to minimize the impact of localized defects. Fig. 9 shows the sampled areas: green regions (1-3) were used to compute the film thickness, whereas the blue square region (6) was used for multiple topographic measurements such as roughness and grain size. Two additional orange regions (4-5) were considered, but later discarded (as detailed below), due to a large amount of defects on the film boundary.

A. Data preprocessing

All the measurements performed on the data acquired through atomic force microscopy (AFM) have been analyzed with the program Gwyddion [25]. A mandatory preliminary step in AFM data analysis is the correction of instrument systematic errors, especially the second-order curvature introduced by the tip actuators. To this aim, we adopted a method similar to the one proposed in [26], where the *median of differences* option in the *align rows* tool is used; this preserves the height of the steps without introducing any significant distortion. Hence, the adopted preprocessing steps for the step evaluation are:

- 1) Subtraction of mean plane
- 2) Correction of horizontal scars
- 3) Alignment of rows with median of differences

Before proceeding, masking was necessary, since the edges of the film were extremely uneven — probably due to a non-ideal lift-off process. We obtained such masks through the *lateral force* tool, as it was able to correctly mark all defects on the edge of the step as well as in the planar regions. Finally, the masks were further expanded through the dilation operation in the *morphological operations* tool in order to add an additional buffer zone around defects.

The step-by-step pre-processing procedure is depicted in Fig. 10 for the region 2 as an example.

The preprocessing method adopted for the topological evaluations is akin to the one used for the step evaluation, except the third step replaced with the *Polynomial* method, that fits a polynomial of given degree and subtracts it from the line, in our case of degree 2.

B. Step height

To determine the step height of our sample, we averaged the values obtained through two different techniques:

- Using the *terraces* tool and incrementally increasing the *step broadening* parameter to $\{0, 1, 2, 3, 4\} \text{ nm}$;
- Fitting the *Boltzman bent step* function on the average of four different profiles on the image.

The measurement was performed using only four images among the available ones due to the presence of strong edge defects that rendered the evaluation inconsistent even within the same image.

The edge defects are most likely due to the lift-off process used to pattern and deposit this film. Further analysis on the relation between the fabrication process and the subsequent effective measured thickness is reported in Appendix D. The data acquired is reported in Table IV and it yields:

$$h = (62.01 \pm 1.69) \text{ nm}$$

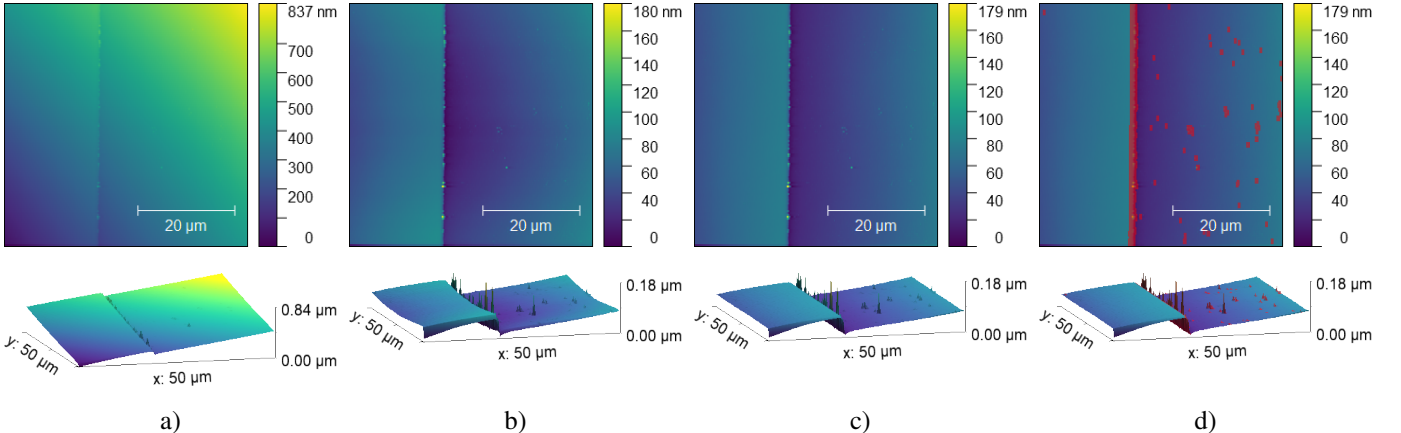


Fig. 10. Effect of different pre-processing steps performed on the collected data, shown for region 2 of Fig. 9. Top row: Topographical image. Bottom row: Corresponding 3D view. a) Unprocessed image b) Mean plane subtraction c) Median of differences d) Masking with lateral force (masked region in red).

This result will be used in Section IV to evaluate the resistivity of the film from its sheets resistance.

C. Roughness

The evaluation of roughness was performed using the *Statistical Quantities* tool of Gwyddion. While this tool allows for a “one-click” result, several considerations must be made regarding the selection of the images and their preprocessing. Reference [27] discusses extensively about the impact of *background removal* tools on the quality of the roughness measurements, showing that, although necessary, these tools alter significantly the results of the roughness analysis. The same work also highlights how the effect of this pre-processing is reduced as the size of the scanned region (i.e. side length L) increases (i.e. magnification decreases), up to the point where it becomes insignificant. Said work also reports that the difference between the measured roughness and the actual one tends to zero for sufficiently low values of the ratio $\alpha = T/L$, where T is the autocorrelation length of the sample.

In order to understand whether our measurements were satisfactory and representative of the actual sample roughness, we measured the *root mean square* roughness ($RMSr$) of different images at different side lengths (10, 5, 3, 2 and 1 μm) and plotted the results in Fig. 11.

With the exception of the highest magnification image ($L = 1 \mu\text{m}$), all the other measurements show a converging behavior, falling within the range $(521 \pm 23) \text{ pm}$ $RMSr$ as the magnification is reduced. Using these results, we can confidently take the value of $RMSr$ measured at 10 μm (averaging the results of the forward and backward scans), giving:

$$RMSr = (529 \pm 23) \text{ pm}$$

A numeric comparison of this result with literature is difficult to make, since the $RMSr$ depends largely on the deposition process² and on the measurement method [27].

²Reference [28] reports a variation of up to 0.9 nm in $RMSr$, depending on the deposition recipe, a lower and upper bound for this value are not found in the literature.

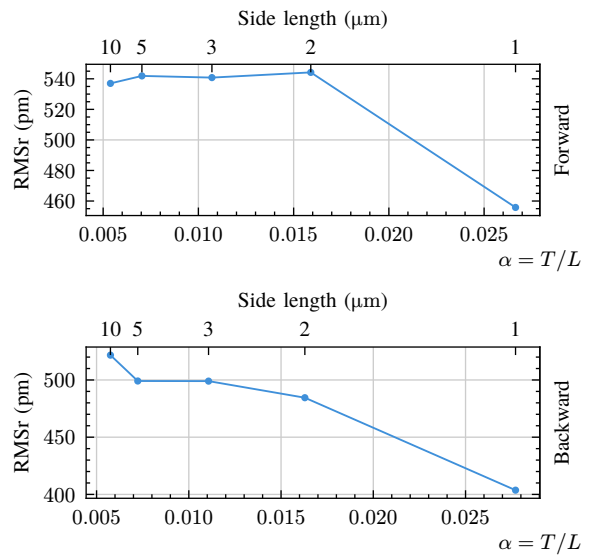


Fig. 11. Relationship between α and the root mean square roughness for both forward (top) and backward (bottom) data. Noticeable converging behavior as α decreases (i.e. L increases).

Nonetheless, even accounting for error in the measurement, we can confidently say that our sample presents low roughness.

D. Grain size

The measurement of the average grain size is a process that is subject both to operator bias and to the applied pre-processing, factors that can significantly alter the final measurement [29]. Although novel methods such as persistent homology (described in the previous reference) have been devised to solve these issues, in this work we will use the tools provided by Gwyddion for the following reasons:

- Given the uniform and overall flat nature of the substrate, minimal pre-processing is required, decreasing the chance of significantly altering the results.
- Tools like watershed and logistic regression have proved to give, in this case, consistent results when compared with each other and with manual selection of the individual grains.

The process of masking and selection of grain boundaries was done starting from the higher resolution images which

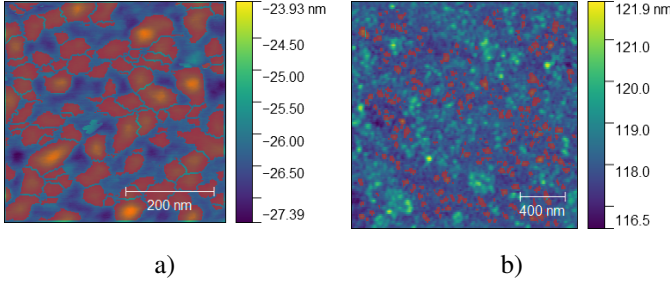


Fig. 12. a) Grains on a high resolution image ($L = 0.5 \mu\text{m}$) marked with the *watershed* method with some manual post-processing. b) Grains on a low resolution image ($L = 2 \mu\text{m}$) marked with a *logistic regression* model trained on image a) and further refined by hand removing large clusters, edge-touching and pixel-sized grains.

allowed to have a *grain size to pixel number ratio* high enough to easily distinguish grains from noise. Within these images, several methods were tested to identify the grains. Here, a brief overview of the results obtained with different methods is reported³:

- *Edge detection*: this method failed to identify grains even on the highest resolution images due to lack of sharp edge boundaries.
- *Otsu's method*: due to the lack of tuning parameters, this method failed to correctly identify most grains, merging higher grain density regions into single larger grains.
- *Mark by threshold*: this method gave better results compared to the previous two but consistently identified only the top-most grains, failing on the ones at lower z height.
- *Watershed*: this method gave significantly better results compared to the previous ones, correctly identifying grains with minimal dependence on their height along the z axis. An example is found in Fig. 12a.
- *Manual selection*: although time consuming, manually tracing the grain contours allowed us to obtain a reference set of measurements to compare other results to, despite being strongly dependent on the user's choice.
- *Logistic regression*: this method allows to transfer segmentation from one image to another one with similar features, or from a small chunk to a complete large image. The method implements a model which needs to be trained on an image with pre-selected grains. After the training process the same model can be used to mark grains on different images. An example is found in Fig. 12b.

The measurement process consisted in measuring the mean grain size (MGS) using watershed and manual selection to get a first set of measurements. Starting from these accurately marked images, logistic regression models were trained to mark lower resolution images to obtain a better statistical sample. Using the measurements shown in Table I (with the exception of the one marked with *), the resulting mean grain size is:

$$\text{MGS} = (28.9 \pm 3.6) \text{ nm}$$

³Most methods required some level of manual post processing to clean the mask, removing false positives grains and removing edge-touching (i.e. partially visible) grains.

TABLE I
M: MANUAL, W: WATERSHED, L: LOGISTIC REGRESSION

Method	$L [\mu\text{m}]$	MGS [nm]
M ^a	0.5	26.8754
M ^a	0.5	25.9878
W ^b	0.5	19.2222 *
W + M ^b	0.5	33.5181
W + M	1	26.6044
W	2	27.6388
W + M	2	26.9242
L + M	3	34.6759

a) Manual selection done by different users

b) Watershed with no manual post processing produces masks where high frequency noise is marked as a multitude of pixel-sized grains, significantly lowering the average grain size. For this reason only the measurement with manual post-processing was considered in the final computation.

The obtained result is well above the threshold of 8 nm described by [30] as the minimum MGS that shows superconducting properties in niobium⁴. An interesting comparison linking grain size and T_c is reported in Section IV.E.

E. Fractal dimension

The surface topography of a thin film typically exhibits fractal properties, indicating a level of irregularity and fragmentation. The fractal dimension (FD) of a profile ranges from 1 to 2, while for a surface, it spans from 2 to 3. A higher FD value signifies greater complexity, irregularity, and enhanced space-filling capability of the topography [33]. Within Gwyddion there are different methods of fractal analysis:

- Cube counting method
- Triangulation method
- Variance (partitioning) method
- Power spectrum method
- Structure function (HHCF) method

The results of different methods differ due to the systematic errors of the different fractal analysis approaches. Averaging the results of different methods applied on all images leads us to the following fractal dimension:

$$\text{FD} = 2.54 \pm 0.27$$

IV. RESISTIVITY AND SUPERCONDUCTIVITY

The electrical properties of the niobium thin film, prepared in a square geometry, were characterized using the Van Der Pauw (VDP) method in a cryogenic environment, with the possibility of introducing a tunable external magnetic field during measurements (see Section IV.E). All measurements were conducted using a four-wire probe configuration to eliminate errors from contact and lead resistance, over a temperature range from 3 K to 296 K.

⁴[31] and [32] disprove such claim, stating that superconducting behavior was observed at grain sizes smaller than 8 nm, suggesting that further analysis must be done in this regard.

A. Resistivity and Pre-processing

The data acquisition process involved a series of measurement cycles, with each cycle yielding two key resistance values, denoted as R_A (horizontal resistance) and R_B (vertical resistance), representing the resistances measured across two orthogonal pairs of contacts on the sample's perimeter. To nullify parasitic thermal voltages, each resistance value was obtained by averaging measurements taken with both forward and reverse current polarities.

Simultaneously, the sample temperature was recorded for each resistance measurement through a temperature controller. This first part of the experiment focused on the normal, non-superconducting regime. Therefore, in order to capture this regime only, we adopted 8 K as a rough threshold temperature between the resistive state and the superconducting transition, which will be investigated instead in Section IV.E.

The orthogonal resistances R_A and R_B are the fundamental parameters required to obtain the sample's sheet resistance, denoted as R_s . The latter is computed by (numerically) solving the Van der Pauw equation (8). For this purpose, we employed the Newton's method on the auxiliary variable $z = 1/R_s$ with relative error tolerance of $5 \cdot 10^{-5}$ and with the first guess z_0 reported in (9).

$$e^{-\pi R_A/R_s} + e^{-\pi R_B/R_s} = 1 \quad (8)$$

$$z_0 = \frac{2 \ln(2)}{\pi(R_A + R_B)} \quad (9)$$

To ensure the thermal stability and validity of each measurement point, the dataset was filtered to select only those pairs of R_A and R_B for which the corresponding temperature fluctuations and absolute temperature difference during the measurement were instrumentally zero.

Upon obtaining the sheet resistance as a function of temperature, the dependence of resistivity on temperature (Fig. 13a) was calculated by multiplying each sheet resistance value by the film's thickness h , determined in Section III.

B. Scattering lifetime and mean free path

Based on the data presented in Fig. 13a, we leveraged the Boltzmann Transport Equation and the Drude model's relaxation time approximation to derive the mean free path l in the normal regime. Within this framework, we considered the electronic band structure to connect conductivity directly to the electronic properties of the film at the Fermi level E_F :

$$\rho^{-1}(T) = \frac{1}{3} q_e^2 \tau \langle v_F^2 \rangle \text{ DOS}(E_F) \quad (10)$$

Inverting (10) and recalling the results from our DFT calculations (see Section II) for the average squared Fermi velocity $\langle v_F^2 \rangle$ and the Density of States at the Fermi level $\text{DOS}(E_F)$, the mean free path for the charge carriers was calculated by multiplying the scattering lifetime by the Fermi velocity: $l(T) = \tau(T) \sqrt{\langle v_F^2 \rangle}$. The result is presented in Fig. 13b.

A comparison of the mean free path of the carriers with the mean grain size (MGS), extrapolated in Section III, reveals that since $l \ll \text{MGS}$, the scattering processes at grain boundaries are negligible with respect to other scattering processes and that intra-grain scattering dominates. This can

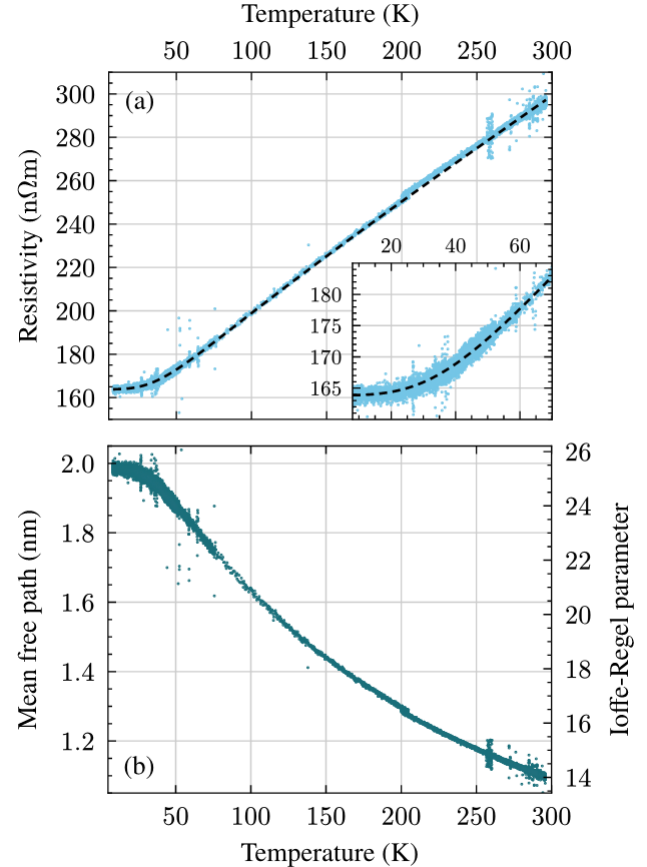


Fig. 13. (a) Resistivity as a function of temperature, in the normal resistive state of niobium. Light blue points represent the experimental data, whereas the dashed black curve represents the fit with the Bloch-Grüneisen model. Three different regimes can be visibly distinguished: a flat region below 20 K due to temperature-independent defects scattering; a power law $\propto T^n$ region up to 60 K and the “normal” linear region, both caused by electron-phonon interaction. (b) Mean free path and Ioffe-Regel parameter as function of temperature.

be confirmed in principle also by comparing the electron wavelength at the fermi level (λ_F) with the MGS [34].

The dominance of intra-grain scattering mechanisms, combined with the extracted mean free path values, suggests enhanced disorder in the present film relative to literature reports. At 10K, [35] and [36] report expected mean free paths above 6 nm for films of similar thicknesses, while [37] measures 9 nm for a 15 nm film. In contrast, at the same temperature, our film exhibits $l \approx 2$ nm, approximately 3-4 times shorter than these literature values.

Finally, the transport quantities obtained in Section II allow us to also evaluate the Ioffe-Regel parameter x . The latter establishes the boundary between coherent, wave-like electron transport and incoherent, diffusive transport. Such criterion states that for a metal to be considered a good conductor, its electronic mean free path must be at least on the order of its Fermi wavelength:

$$x = k_F \cdot l = \frac{E_F \tau}{\hbar} \geq 1 \quad (11)$$

To calculate this parameter for our material, we employ the value of Fermi energy $E_F = 5.893 \text{ eV}$ obtained from our theoretical calculations in Section II.A.

The results of Fig. 13b show that the parameter remains well above the critical value of 1 across the entire measured temperature range, confirming the material's nature as a good metallic conductor.

Furthermore, this behavior is consistent with the increasing dominance of electron-phonon scattering at higher temperatures, which shortens the electron mean free path and, consequently, reduces the Ioffe-Regel parameter.

C. Residual resistivity ratio

The Residual-Resistivity Ratio, RRR, serves as a quantitative measure of the film's crystalline quality and purity. It is defined as the ratio of the resistivity at room temperature (ρ_{300}) to the residual resistivity (ρ_0) exhibited at low temperatures just above the superconducting transition.

To determine these values, we first analyzed the sheet resistance curve as a function of temperature. The residual sheet resistance, R_{S0} , was calculated by identifying the low-temperature plateau of the curve, from temperatures of approximately 8K upwards. This region corresponds to the film's normal state before the onset of superconductivity. A derivative method was used to select the points on the curve with a first derivative below a precise experimental threshold, confirming their presence on the flat plateau. A linear fit of the form $y = c$ was then applied to this portion of the data, with the coefficient c representing R_{S0} . The result for the residual sheet resistance was determined to be $R_{S0} = (2.643 \pm 0.012) \Omega/\text{sq}$.

Similarly, the sheet resistance at room temperature, R_{S300} , was determined from the high-temperature portion of the curve. All data points in the region above 200K were fitted with a linear function, extended to a temperature of 300K. This yielded a value of $R_{S300} = (4.813 \pm 0.007) \Omega/\text{sq}$.

Using these values, the Residual-Resistivity Ratio turns out to be in the order of the unity:

$$\text{RRR} = \frac{\rho_{300}}{\rho_0} = \frac{R_{S300}}{R_{S0}} = 1.821 \pm 0.009 \quad (12)$$

Although especially pure, bulk niobium can exhibit very large RRR (up to the order of 10^4) [38], much lower values may be expected for less pure films. For instance, [37] reports an RRR of 6.5 for a 15 nm thick film, while [35] measured RRR values of 3.074 and 4.103 for 50 nm and 62 nm films, respectively. Further discussions regarding the influence of RRR with mean free path and critical temperature are reported in Section IV.E.

D. Bloch-Grüneisen model

In order to describe now the resistivity contribution arising from different electron-phonon scattering mechanisms, the Bloch-Grüneisen (BG) model provides a theoretical framework that can be expressed as:

$$\rho(T) = \rho_0 + A \left(\frac{T}{\Theta_{BG}} \right)^n \int_0^{\Theta_{BG}/T} \frac{t^n dt}{(e^t - 1)(1 - e^{-t})} \quad (13)$$

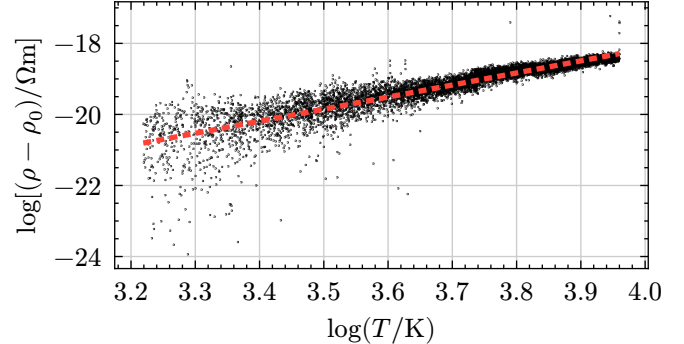


Fig. 14. Logarithmic plot of the temperature-dependent resistivity, $\rho - \rho_0$, versus temperature. The data points were isolated from the power-law region of the raw resistivity curve using the derivative method. The slope of the linear fit to this logarithmic plot provides an initial estimate for the Bloch-Grüneisen exponent n .

where ρ_0 is the residual resistivity, A is a constant related to the electron-phonon coupling strength and Θ_{BG} is the Bloch-Grüneisen characteristic temperature. Finally, n is the exponent that governs the temperature-dependent power-law behavior of resistivity in the crossover region between the low-temperature residual resistivity plateau and the high-temperature linear regime.

Directly fitting this complex equation to the entire experimental dataset can be challenging. To facilitate convergence, an initial estimate for the exponent n was first determined. For this purpose, we applied the derivative method to the resistivity curve of Fig. 13 to isolate the data points within the crossover region, which is characterized by a rapidly changing, non-constant derivative, well distinct from the constant derivatives of the low and high-temperature zones. On this selected data, we performed a linear fit on the plot of $\log(\rho - \rho_0)$ versus $\log(T)$ – Fig. 14. The slope of this fitted line gave us the initial estimate $n = 3.398$ for the complete Bloch-Grüneisen.

With the residual resistivity $\rho_0 = R_{S0}h$ set to its experimentally determined value, the Bloch-Grüneisen equation was then fitted to the full dataset (dashed curve in Fig. 13a). The fitting process successfully converged, providing the following optimized parameters:

- $n = 3.592 \pm 0.022$
- $A = (2.908 \pm 0.026) \cdot 10^{-7} \Omega \text{ m}$
- $\Theta_{BG} = (259.98 \pm 0.01) \text{ K}$.

The power n can give us insights on the nature of the dominant scattering mechanism in our sample. In fact, despite the notable contribution from grain morphology to electronic scattering, the analysis reveals that the temperature-dependent resistivity in our Niobium film is primarily dominated by *s-d* inter-band scattering rather than *s-s* intra-band mechanisms, as previously observed in literature [38], [39], [40]. This argument is further justified by the noticeable difference of the average Fermi velocity between the two bands crossing the Fermi energy, which are respectively $4.36 \cdot 10^5 \text{ m s}^{-1}$ and $7.40 \cdot 10^5 \text{ m s}^{-1}$, as computed by DFT. Nonetheless, n turns out to be slightly greater than 3, which may suggest a non-negligible contribution due to intra-band scattering of electrons with acoustic phonons.

Also the Bloch-Grüneisen temperature Θ_{BG} matches our expectation. Indeed, it turns out to be close to the experimental value of the Debye temperature of niobium, around 276 K [18] and 275 K [19]. This is the expected value since the Fermi surface of niobium (Fig. 4) fully occupies the Brillouin zone, thus allowing a big fraction of acoustic phonons to scatter off electrons.

Combining the notion of Θ_{BG} and of the critical temperature (see Section IV.E), it is possible to invert the original McMillan formula and obtain the thermodynamic electron-phonon coupling constant:

$$\lambda_{th} = \frac{1.04 + \mu^* t}{(1 - 0.62\mu^*)t - 1.04} = 1.080 \pm 0.002 \quad (14)$$

where $t = -\ln(1.45 T_c / \Theta_{BG})$ and $\mu^* = 0.24$ is the empirical Morel-Anderson pseudo-potential [12]. Although incompatible with DFPT results (Section II.C), it is compatible with the experimental value 1.14 ± 0.07 obtained from the mass enhancement factor $(1 + \lambda_{th})$ through de Haas-van Alphen effect [12].

Finally, starting from the pre-factor A it is possible to extrapolate the transport electron-phonon coupling constant λ_{tr} , which describes the strength of the interaction between conduction electrons and lattice vibrations. Indeed, under the assumption of a Debye transport spectral function employed by the Bloch-Grüneisen model, electron-phonon scattering theory implies the following relation:

$$A = \frac{8\pi V_{cell} m^*}{N_v q_e^2 \hbar} k_B \Theta_{BG} \lambda_{tr} \quad (15)$$

Upon inversion, (15) leads us to the value $\lambda_{tr} = 1.278 \pm 0.011$. Although compatible with DFPT results, this value is noticeably bigger than previous findings in literature, reporting values around $\lambda_{tr} \approx 1.06$ [41], [42]. Another issue with the derived value of λ_{tr} is that it is bigger than λ_{th} , whereas the opposite should occur, due to small-angle scattering. Since our DFPT calculations are not fully converged, we deem a comparison with the numerical λ to be unreliable⁵. We therefore attribute the error in our experimental λ_{tr} to the contribution of m^* and Θ_{BG} in (15), being the most inaccurate quantities.

E. Superconducting Transition

After a comprehensive analysis of the normal state properties of the niobium thin film, in this section we focus on its superconducting behavior at low temperatures. Using the same experimental setup and Van Der Pauw measurement technique, we collected data down to a minimum temperature of 3 K. For each measurement cycle, the corresponding sheet resistance was calculated from the two orthogonal resistances, R_A and R_B using the same procedure previously described.

To investigate the influence of an external magnetic field on the superconducting transition, we systematically varied the magnetic flux density B applied on the sample and measured the sheet resistance as a function of temperature. These measurements allowed us to confirm the suppression of the

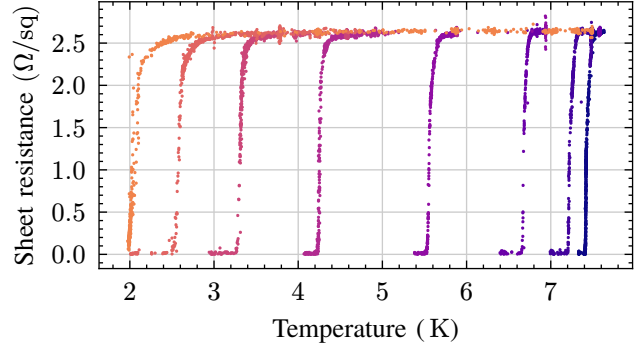


Fig. 15. Sheet resistance as a function of temperature around the superconductive transitions. Colors from dark purple to orange represent increasing value of magnetic flux density $B \in \{0, 0.4, 0.8, 1.6, 2.4, 3.2, 3.6\}$ T. Increasing the magnetic flux visibly decreases the critical temperature T_c as well as broadening the transition.

critical temperature T_c with increasing magnetic field, a well-known characteristic of superconducting materials. Fig. 15 depicts the superconducting transition of our niobium sheet for different applied B . We highlight that we were not able to observe a full superconducting transition at $B = 3.8$ T, as the cryostat's minimum achievable temperature of 2 K was not low enough to capture its base. We also acknowledge the progressive broadening of the transitions with B , rendered in Fig. 16. For bulk materials this is traditionally associated to flux-flow phenomenon and inhomogeneity, whereas for smooth (RMS < 1 nm) thin films with parallel magnetic field, as in our case, it can be primarily attributed to the residual surface superconductivity. In particular, the latter affects the broadening of the topmost part of the transition, while the influence of bulk effects impacts its base [43], [44].

Starting from this overview, we now delve into the characterization of the critical temperature. After normalizing the sheet resistance with respect to R_{S0} , the critical temperature was then formally defined as the temperature at which the normalized resistance reaches 50% of its normal-state value, i.e. $R_s/R_{S0} = 1/2$. The half difference between the temperatures corresponding to 10% and 90% of the transition was used to quantify the uncertainty associated to T_c . The result of this procedure is depicted in Fig. 16 for all the values of applied field. For $B = 0$ T we obtain $T_c = (7.426 \pm 0.040)$ K.

To explain the difference between the obtained value and the one accepted in the literature for pure bulk niobium of 9.3 K ([23], [24]), we can take into account the impact that film thickness and grain size have on T_c . Regarding the effect of film thickness, various works ([35], [36], [45]) show that a decrease in film thickness causes a reduction of the critical temperature. While this trend could qualitatively explain the experimental results of this work, the measured reduction in T_c is too large to be attributed to this effect only: as an example, for films with thickness comparable to ours (50 nm and 62 nm), [35] reports critical temperatures of, respectively, 8.6 K and 8.9 K. As anticipated, the grain size of the sample also plays an important role in the behavior of the critical temperature; reference [30] investigates this relationship on

⁵Indeed, using 16×3 k - and q -grids, [21] derived $\lambda_{th} = 1.057$ which is close to experimental result of [12] and of our work.

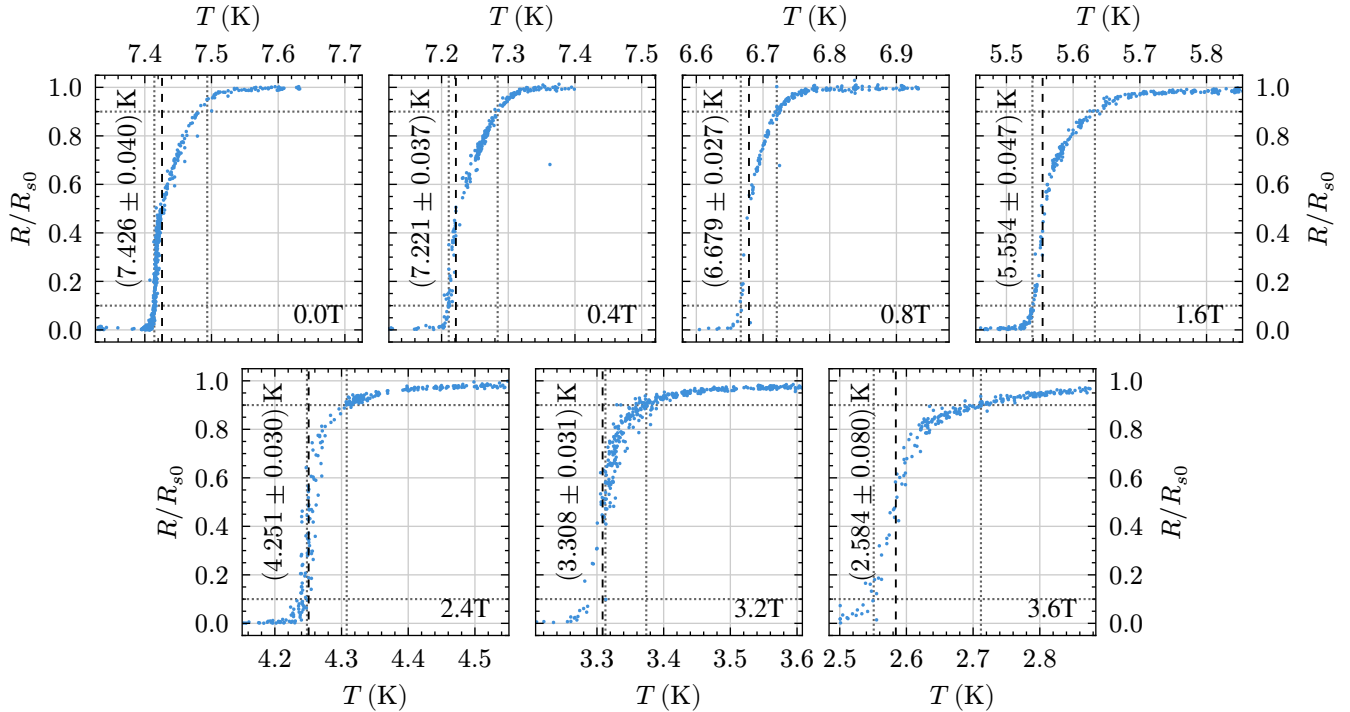


Fig. 16. Normalized sheet resistance R_s/R_{s0} as a function of temperature for different applied magnetic fields (lower right corner). The critical temperature T_c is defined as the temperature at which the normalized resistance reaches 50% of its normal-state value. The uncertainty is quantified as the half-difference between the temperatures corresponding to the 10% and 90% points of the transition, indicated by the faint dotted lines.

a 500 nm Nb film⁶ by performing electrical measurements for films with different grain size. For example, for mean grain sizes of 28 nm, 19 nm, and 11 nm, the reported critical temperatures are 9.3 K, 7.8 K, and 5.9 K, respectively.⁷

Again, while our sample also has a limited mean grain size, the T_c difference from the reference values is too large to be attributed to such effect alone, even accounting for possible measurement errors or methodology difference with respect to the references.

Therefore we believe that, although both reported phenomena could likely contribute to the reduction in T_c , the dominant suppression factor in our sample is best attributed to crystalline disorder, consistent with the already extracted short mean free path and the low RRR relative to state-of-the-art niobium thin films.

F. Critical Field versus Critical Temperature

We now focus on the full width of the superconducting transition. To this aim, we identify two additional characteristic temperatures: the onset of the transition, T_c^{on} , and the point where the resistance reaches zero, T_c^{zero} . To mitigate the effects of experimental noise and ensure a robust analysis, the thresholds for these temperatures were defined at slightly

higher and lower values than the ideal 1% and 99% marks, being 3% and 97% respectively.

The observed trends of T_c , T_c^{on} , and T_c^{zero} as function of B can be described by the results of the Ginzburg-Landau (GL) theory, which provides a phenomenological framework for understanding superconductivity near the critical temperature. A simplified extension of this model, often used to fit experimental data, relates the upper critical field $B_{c,2}$ to the temperature T via the expression:

$$B_{c,2}(T) = B_{c,2}(0) \frac{T_c^2 - T^2}{T_c^2 + T^2} \quad (16)$$

where T_c is intended as the mean-field critical temperature, and $B_{c,2}(0)$ is the upper critical field at absolute zero. By fitting $B_{c,2}(T)$, $B_{c,2}^{\text{zero}}(T)$, $B_{c,2}^{\text{on}}(T)$ to this model, we can map out the superconducting phase diagram – Fig. 17 – which depicts the boundary between the normal and superconducting states. The black line represents the phase diagram associated with T_c ; however, this parameter falls in the middle of the superconductive transition, halfway between the superconductive and normal regimes, so it can not be treated as the actual neat bound between the two. The blue line (T_c^{zero}) can be regarded as the upper bound for the full coherence of GL superconductive parameter $\Psi(\vec{r})$, while the orange line (T_c^{on}) as the lower bound of the normal state. The intermediate regions feature a progressive loss in the coherence of $\angle\Psi(\vec{r})$ starting from T_c^{zero} and of $|\Psi(\vec{r})|$ from T_c to T_c^{on} , resulting in the motion of fluxons and fluctuation of cooper pairs density [43], [44].

From the present analysis, it is also possible to derive the material's coherence length. Within the framework of

⁶Despite the large difference in thickness between the two samples we believe this comparison to be valid since they can both be considered 3D samples [35].

⁷Since the exact values are not reported in the cited work, the data has been obtained from the plots. Despite unavoidable inaccuracies of this method, we believe that this information is nonetheless valuable for the point in question.

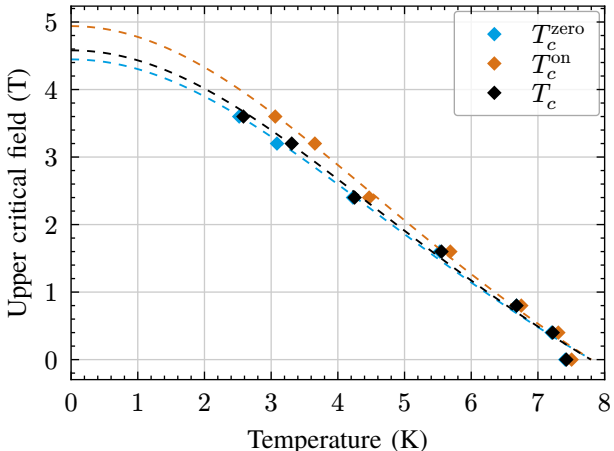


Fig. 17. Phase diagram of niobium superconductive transition, tracking the interdependency of critical temperature and critical magnetic field. Dots represent the experimental data, dashed lines the fits according to (16). While GL theory should be most precise for $T \sim T_c$, we notice how the theoretical trend still fails in reproducing the experimental data: we attribute this distortion of the phase-diagram to the influence of surface superconductivity induced by the parallel orientation of the magnetic field [44], [46].

the Ginzburg-Landau theory, the coherence length ξ_0 of the superconductive order parameter is related to the upper critical magnetic field through the equation (17), where Φ_0 is the fundamental magnetic flux quantum.

$$\xi_0 = \sqrt{\frac{\Phi_0}{2\pi B_{c,2}(0)}} \quad (17)$$

After recovering $B_{c,2}(0) = (4.55 \pm 0.04)$ T by the fit in Fig. 17, we finally derive the value $\xi_0 = (8.50 \pm 0.04)$ nm, which is close to past findings [47], [48] – reporting an increase of ξ_0 with respect to film thickness h and $\xi_0 \approx 12$ nm at $h = 50$ nm, unknown grain size – but still underestimated. Indeed an additional role could be played by the grain size itself, which has been demonstrated to decrease the coherence length at constant film thickness [49]. Moreover, we attribute our lower value of ξ_0 also to the overestimation of $B_{c,2}(0)$ as a fit parameter, which could have been improved by acquiring additional data for the fit at higher applied field.

Finally, we conclude that our sample is in the dirty limit since the mean free path is substantially lower than the coherence length.

V. CONCLUSIONS

In this work, we employed a multi-faceted experimental approach to comprehensively characterize the electrical, phononic, superficial, and superconductive properties of our microfabricated thin film niobium sample. The AFM analysis detailed in Section III reported the most common procedures among various methods to obtain plausible final values of roughness and grain size, and highlighted the main defects of the sample on the stripped borders. Ab-initio crystal computation in Section II confirmed the expected trends of electronic and phononic bands and density of states, whereas quantities related to electron-phonon interaction turned out to be less satisfactory. For the latter, bigger sampling k - and q -

grids are needed to increase the simulation accuracy. Finally, the analysis in Section IV of the experimental measurements of the film resistance lead to many macroscopic quantities reasonably compatible with expectations and past findings in literature. Nonetheless, we reported a critical temperature substantially lower than the accepted value in literature: we mainly attribute this issue to the partial impurity of our sample (highlighted by low RRR), to its low-dimensionality and grain size.

APPENDIX A: FERMI VELOCITY AND EFFECTIVE MASS

The result of DFT is the ground-state electron density and wavefunction. For each band, these can be sampled on an arbitrary k -grid — here, $72 \times 72 \times 72$ — to obtain the eigenenergies at such points (in ABINIT, this is the XCrysDen BXSF file). Using this data, it is possible to numerically reconstruct the Fermi surface profile by employing the Marching Cubes algorithm to construct the triangular mesh of the isosurface with energy equal to E_F . By means of numerical integration, it is then possible to average any quantity on this approximation of the Fermi surface.

The quantities we wish to average are the Fermi velocity and effective mass, which depend on the first and second derivative of E with respect to k . We expect finite difference methods to give poor results since the k -grid is relatively coarse. Therefore, we opted to avoid them in favor of using interpolating cubic functions, which we can then sample arbitrarily. Another advantage of a cubic interpolant is that its gradient and hessian are both analytical and easy to compute.

The complete procedure is the following:

- 1) The triangular mesh of the isosurface at E_F is constructed using the Marching Cubes algorithm;
- 2) The volumetric data of $E(\vec{k})$ is interpolated using cubic B-splines with periodic boundary conditions;
- 3) v_F and m_{eff} are integrated on the triangles of the mesh using Gauss-Legendre quadrature with 3 points;
- 4) The final average value is then obtained by dividing the previous integral with the total area of the surface.

For what concerns the Fermi velocity, since its value is employed in conduction-related formulas, we are interested in its magnitude square — $\|v_F\|^2 = \|\nabla_k E\|^2$ — which is a scalar and thus straightforward to average. On the other hand, the computation of the effective mass deserves more attention. The inertial mass is in general a tensor (18) which depends on the position in the reciprocal space, and thus cannot be simply integrated on the Fermi surface.

$$M_{\text{inert}}(\vec{k}) = \hbar^2 [\nabla_k \nabla_k E(\vec{k})]^{-1} \quad (18)$$

Indeed, the speed of an electron will depend on its direction, which in general is not aligned with the direction of the forcing electric field. However, many conduction-related calculations require a single scalar value for the effective mass. As the conductivity of any material is inversely proportional to the effective masses, one finds that the conductivity due to multiple contributions is proportional to the sum of the inverse of the individual masses. Therefore, we will compute

the average on the Fermi surface of the arithmetic mean of the eigenvalues of $M_{\text{inert}}^{-1}(\vec{k})$, which simplifies to averaging $\text{tr}[\nabla_k \nabla_k E]/(3\hbar^2)$. This operation is performed on the sheets of the Fermi surface on the second and third Brillouin zones, producing two values of $\langle m_{\text{eff}}^{-1} \rangle$ which are then averaged based on the carrier contribution of each sheet – in our case, two electrons each. The results are reported in Table II.

TABLE II

FERMI VELOCITY AND EFFECTIVE MASS IN EACH BRILLOUIN ZONE AND ON THE OVERALL FERMI SURFACE, WHOSE SURFACE AREA IS REPORTED NORMALIZED TO THE RELAXED LATTICE CONSTANT

	v_F [10 ⁵ m/s]			$\frac{m_{\text{eff}}}{m_e}$	$a_{\text{rlx}}^2 S$
	min	avg	max		
2 nd BZ	2.652	4.385	8.660	-1.039	1.020
3 rd BZ	1.902	7.225	12.326	-12.273	9.655
Total	1.902	7.004	12.326	-2.088	10.675

APPENDIX B: DEBYE TEMPERATURE FROM DOS_{ph}

Once acquired the phonon density of states, our objective is to find the most parabolic window at the start of the curve, so that we can extrapolate an equivalent Debye temperature. To this aim, we adopted the following procedure:

- 1) Consider the range $[0, \omega_T]$ with $\omega_T > 0$
- 2) Fit the function $\beta\omega^2$ to the DOS_{ph} on such range
- 3) Compute the coefficient of determination R^2
- 4) Repeat the previous steps for all $\omega_T \in (0, 2]$ THz
- 5) Choose the fit with the highest R^2 and derive the Debye temperature from its parameter β :

$$\Theta_D = \sqrt[3]{\frac{3}{\beta} \int_0^\infty \text{DOS}_{\text{ph}}(\omega) d\omega} = \sqrt[3]{\frac{9}{\beta}}$$

APPENDIX C: 18^{×3} k- AND 6^{×3} q-GRID CONFIGURATION

For completeness we also report the results obtained using 18^{×3} k - and 6^{×3} q -grids. Although the convergence with respect to k -grid is reasonably reached, we reckon the 6^{×3} q -grid to be too small. This is clear by looking at Fig. 18 and Fig. 19:

- Although close to the experimental bands around Γ , the computed phonon bands are visibly shifted and partially distorted;
- The peaks of the computed Eliashberg function do not align with the experimental ones, and its magnitude is greatly overestimated;
- The Eliashberg function is non-zero for some negative values of ω , which is a non-physical result.

Moreover, we report that many self-consistent cycles were not able to reach the target tolerance within the maximum number of iterations allowed (which was necessary, since the computation took 12 days to complete).

Table III reports various quantities derived from phonon bands, phonon density of states, and Eliashberg function for both grid configurations.

APPENDIX D: STEP EVALUATION DATA

Table IV presents the measurements used to determine the mean step height. For each image, the reported mean and standard deviation values are the average of the results obtained from the *terraces* tool (h_A row) and the average across all methods (row h_B). In this regard, we made two relevant observations regarding the following aspects:

- The creep and hysteresis due to the piezoactuators [50].

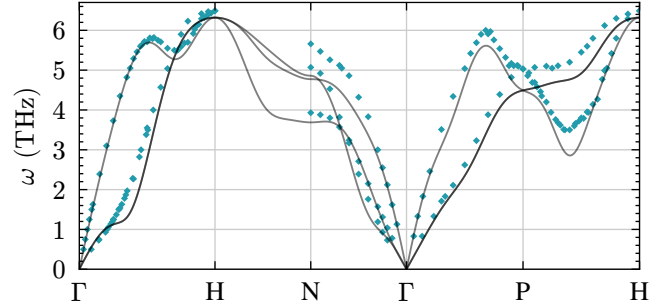


Fig. 18. Phononic states of niobium, obtained using a 18×3 k -grid and a 6×3 q -grid. Although close, the computed bands (solid black) are visibly shifted from the experimentally measured ones [16], reported in cyan.

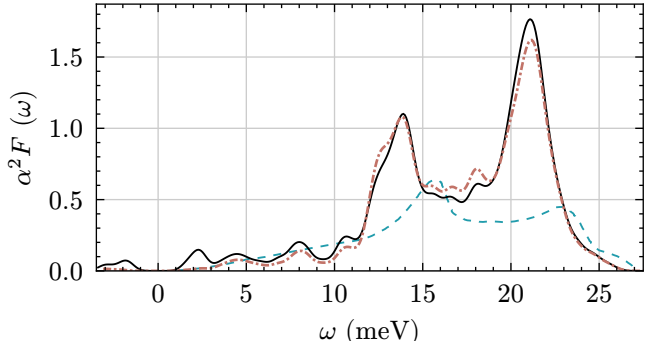


Fig. 19. Electron-phonon spectral (Eliashberg) function as function of phonon frequency, obtained using a 18×3 k -grid and 6×3 q -grid. The blue dashed line represent the experimental (superconducting) $\alpha^2 F$ obtained through proximity electron tunneling spectroscopy [20]. The solid black and dash-dotted red curves are respectively the thermodynamic and transport electron-phonon spectral functions $\alpha_{\text{th}}^2 F$ and $\alpha_{\text{tr}}^2 F$.

TABLE III
VARIOUS QUANTITIES DERIVED FROM THE PHONON BANDS, THE PHONON DOS, AND THE ELIASHBERG FUNCTION, FOR THE TWO GRID CONFIGURATIONS.

k -grid	18 ^{×3}	12 ^{×3}
q -grid	6 ^{×3}	12 ^{×3}
$v_{s,1}$	1.79	2.06
$v_{s,2}$	2.09	2.78
$v_{s,3}$	4.68	4.67
$v_{s,\text{avg}}$	2.85	3.17
Θ_D	247.7	235.6
λ_{tr}	1.379	1.277
λ_{th}	1.744	1.350
$\omega_{\log}^{\text{th}}$	2.424	3.251
T_c	9.788	8.844
		K
		/

TABLE IV
ALL MEASUREMENTS IN nm UNLESS OTHERWISE SPECIFIED

Region / Direction	Measurements				$\langle h_{A/AB} \rangle$	$\sigma_{A/AB}$
2 / FRW	Step Broad. [μm]	0	1	2	3	
	h_A	63.0179	62.8621	63.1809	63.7126	63.19
	h_B	63.01			63.16	0.33
2 / BKW	Step Broad. [μm]	0	1	2	3	
	h_A	60.23	60.3645	60.4311	60.8375	60.47
	h_B	61.41			60.65	0.48
1 / BKW	Step Broad. [μm]	0	1	2	3	
	h_A	60.7912	60.7265	60.7443	61.0896	60.84
	h_B	61.71			61.01	0.41
3 / FRW	Step Broad. [μm]	0	1	2	3	
	h_A	63.1279	63.0359	63.2671	63.6604	63.27
	h_B	63.05			63.23	0.26
4 / FRW not used in measurement	Step Broad. [μm]	0	1	2	3	
	h_B	32.5913	32.7649	31.8416	31.1499	32.09
	h_B	/			/	/

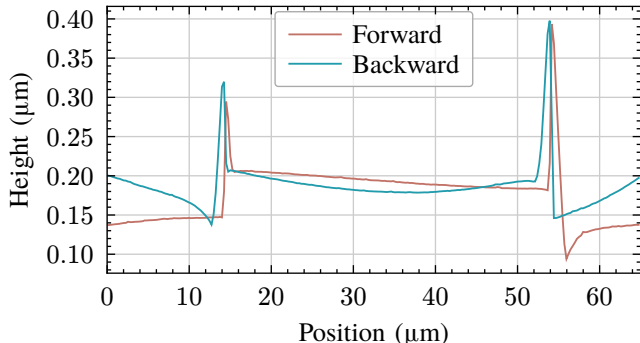


Fig. 20. Profile of the scanned region 4 along the transversal axis. Creep effects are evident, and, as expected, direction-dependent. These profiles are derived from an image which was eventually discarded (as detailed in Section III.A), but still reported here as a clear example of hysteresis.

- The difference in thicknesses in different regions.

The profiles of the scanned regions exhibit a notable creep effect, as illustrated in Fig. 20. This phenomenon occurs due to the behavior of the piezo-actuator, which continues to deform under the applied voltage. Importantly, the actuator does not instantly return to its original strain level upon disconnection from the voltage source. This delayed recovery can lead to inaccuracies in the measurement of the thin film's properties. Since the creep is a directional effect, we considered four measurements to evaluate the average thickness: two taken in the forward direction and two in the backward direction. In our opinion, this approach should be sufficient to average out the issue, allowing us to assume that our measured value is acceptable for further evaluations. From Table IV, we can see that the forward measurements differ from the backward ones by more or less 3 nm. We suspect that this fact may be related to the hysteresis, which can arise in piezoactuators from various factors such as the nonlinear response of the

actuator. While the hysteresis effect should be compensated by the hardware position correction in our instrument, the profile still displays significant curvatures and discrepancies in the steps between the forward and backward readings, even after preprocessing to remove background bowing and other factors. These findings may stem from the previously mentioned effects, as well as additional anomalies.

From Table IV, we can observe that the measurements taken from the same image using different methods are consistent, and all analyzed measurements are within approximately 3 nm. However, there is a discrepancy in the measurement from region 4 (corresponding to the narrow strip in Fig. 9). The measurement obtained with the terraces tool in this region gives an average thickness of (32.09 ± 0.74) nm, which is nearly half of the thickness measured in other regions, while with the other method we were not able to properly fit the function, even after the masking. This inconsistency may be attributed to the deposition process used: the thin film was patterned through a lift-off process and deposited via magnetron sputtering. This process involves using a sacrificial layer, typically a photoresist, which requires an undercut to effectively deposit the material in the desired pattern. Any issues during this process may lead to uneven deposition, hence uneven thicknesses, especially between features with different aspect ratios, resulting in differences in height and edge defects (as shown in Fig. 20), rendering the measurements in these regions less significant.

Since the sample used for the resistivity measurement was geometrically more similar to the wider part of the sample analyzed with the AFM, we believe that the reported thickness is acceptable for resistivity evaluations. However, it is important to note that inconsistencies between our evaluations and the literature may arise due to the actual differences in thickness.

REFERENCES

- [1] C. Antoine, *Materials and surface aspects in the development of SRF Niobium cavities*. in EuCARD editorial series on accelerator science. 2012. [Online]. Available: <https://cds.cern.ch/record/1472363>
- [2] G. Myneni *et al.*, “Medium grain niobium SRF cavity production technology for science frontiers and accelerator applications,” *Journal of Instrumentation*, vol. 18, no. 4, p. T4005, Apr. 2023, doi: 10.1088/1748-0221/18/04/T40005.
- [3] A. J. Annunziata *et al.*, “Reset dynamics and latching in niobium superconducting nanowire single-photon detectors,” *Journal of Applied Physics*, vol. 108, no. 8, 2010.
- [4] G. Gol'tsman *et al.*, “Middle-Infrared to Visible-Light Ultrafast Superconducting Single-Photon Detectors,” *IEEE Transactions on Applied Superconductivity*, vol. 17, no. 2, pp. 246–251, 2007, doi: 10.1109/TASC.2007.898252.
- [5] M. Faucher *et al.*, “Niobium and niobium nitride SQUIDs based on anodized nanobridges made with an atomic force microscope,” *Physica C: Superconductivity*, vol. 368, no. 1–4, pp. 211–217, 2002.
- [6] A. G. Troeman, H. Derking, B. Borger, J. Pleikies, D. Veldhuis, and H. Hilgenkamp, “NanoSQUIDs based on niobium constrictions,” *Nano Letters*, vol. 7, no. 7, pp. 2152–2156, 2007.
- [7] W. Chen, V. Patel, S. K. Tolpygo, D. Yohannes, S. Pottorf, and J. E. Lukens, “Development toward high-speed integrated circuits and SQUID qubits with Nb/AlO/sub x/Nb Josephson junctions,” *IEEE transactions on applied superconductivity*, vol. 13, no. 2, pp. 103–106, 2003.
- [8] M. Bal *et al.*, “Systematic improvements in transmon qubit coherence enabled by niobium surface encapsulation,” *npj Quantum Information*, vol. 10, no. 1, p. 43, 2024.
- [9] J. W. Arblaster, *Selected values of the crystallographic properties of elements*. ASM International, 2018.
- [10] L. F. Mattheiss, “Electronic Structure of niobium and Tantalum,” *Phys. Rev. B*, vol. 1, no. 2, pp. 373–380, Jan. 1970, doi: 10.1103/PhysRevB.1.373.
- [11] A. R. Jani, N. E. Brener, and J. Callaway, “Band structure and related properties of bcc niobium,” *Phys. Rev. B*, vol. 38, no. 14, pp. 9425–9433, Nov. 1988, doi: 10.1103/PhysRevB.38.9425.
- [12] G. B. Scott and M. Springfield, “The Fermi surface in niobium,” *Proc. R. Soc. Lond. A*, vol. 320, pp. 115–130, 1970, doi: 10.1098/rspa.1970.0200.
- [13] M. H. Halloran, J. H. Condon, J. E. Graebner, J. E. Kunzler, and F. S. L. Hsu, “Experimental Study of the Fermi Surfaces of niobium and Tantalum,” *Phys. Rev. B*, vol. 1, no. 2, pp. 366–372, Jan. 1970, doi: 10.1103/PhysRevB.1.366.
- [14] A. K. Solanki, R. Ahuja, and S. Auluck, “Fermi Surface and Mass Enhancement Factor for niobium,” *physica status solidi (b)*, vol. 162, no. 2, pp. 497–507, 1990, doi: <https://doi.org/10.1002/pssb.2221620221>.
- [15] L. F. Mattheiss, “Fermi Surface in Tungsten,” *Phys. Rev.*, vol. 139, no. 6A, pp. A1893–A1904, Sep. 1965, doi: 10.1103/PhysRev.139.A1893.
- [16] B. Powell, P. Martel, and A. Woods, “Phonon properties of niobium, molybdenum, and their alloys,” *Canadian Journal of Physics*, vol. 55, pp. 1601–1612, 2011, doi: 10.1139/p77-204.
- [17] G. V. Samsonov, *Handbook of the Physicochemical Properties of the Elements*. Springer Science & Business Media, 2012.
- [18] G. R. Stewart, “Measurement of low-temperature specific heat,” *Review of Scientific Instruments*, vol. 54, no. 1, pp. 1–11, 1983, doi: 10.1063/1.1137207.
- [19] B. J. C. van der Hoeven and P. H. Keesom, “Specific Heat of niobium between 0.4 and 4.2 K,” *Phys. Rev.*, vol. 134, no. 5A, pp. A1320–A1321, Jun. 1964, doi: 10.1103/PhysRev.134.A1320.
- [20] E. L. Wolf, J. Zasadzinski, J. W. Osmun, and G. B. Arnold, “Proximity electron tunneling spectroscopy I. Experiments on Nb,” *Journal of Low Temperature Physics*, vol. 40, pp. 19–50, 1980, doi: 10.1007/BF00115980.
- [21] M. Zarea, H. Ueki, and J. A. Sauls, “Effects of anisotropy and disorder on the superconducting properties of niobium,” *Frontiers in Physics*, vol. 11, Oct. 2023, doi: 10.3389/fphy.2023.1269872.
- [22] B. N. Harmon and S. K. Sinha, “Electron-phonon spectral function and mass enhancement of niobium,” *Phys. Rev. B*, vol. 16, no. 9, pp. 3919–3924, Nov. 1977, doi: 10.1103/PhysRevB.16.3919.
- [23] D. K. Finnemore, T. F. Stromberg, and C. A. Swenson, “Superconducting Properties of High-Purity niobium,” *Phys. Rev.*, vol. 149, no. 1, pp. 231–243, Sep. 1966, doi: 10.1103/PhysRev.149.231.
- [24] S. J. Williamson, “Bulk Upper Critical Field of Clean Type-II Superconductors: V and Nb,” *Phys. Rev. B*, vol. 2, no. 9, pp. 3545–3556, Nov. 1970, doi: 10.1103/PhysRevB.2.3545.
- [25] D. Nečas and P. Klapetek, “Gwyddion: an open-source software for SPM data analysis,” *Central European Journal of Physics*, vol. 10, no. 1, pp. 181–188, 2012, doi: 10.2478/s11534-011-0096-2.
- [26] J. Garnæs *et al.*, “Algorithms for using silicon steps for scanning probe microscope evaluation,” *Metrologia*, vol. 57, no. 6, p. 64002, Oct. 2020, doi: 10.1088/1681-7575/ab9ad3.
- [27] D. Nečas, P. Klapetek, and M. Valtr, “Estimation of Roughness Measurement Bias Originating from Background Subtraction,” *Measurement Science and Technology*, vol. 31, no. 9, p. 94010, Sep. 2020, doi: 10.1088/1361-6501/ab8993.
- [28] X. Li, W. H. Cao, X. F. Tao, L. L. Ren, L. Q. Zhou, and G. F. Xu, “Structural and Nanomechanical Characterization of niobium Films Deposited by DC Magnetron Sputtering,” *Applied Physics A*, vol. 122, no. 5, p. 505, May 2016, doi: 10.1007/s00339-016-9990-1.
- [29] A. N. Duman, “Grain Analysis of Atomic Force Microscopy Images via Persistent Homology,” *Ultramicroscopy*, vol. 220, p. 113176, Jan. 2021, doi: 10.1016/j.ultramic.2020.113176.
- [30] S. Bose, P. Raychaudhuri, R. Banerjee, P. Vasa, and P. Ayyub, “Mechanism of the Size Dependence of the Superconducting Transition of Nanostructured Nb,” *Physical Review Letters*, vol. 95, no. 14, p. 147003, Sep. 2005, doi: 10.1103/PhysRevLett.95.147003.
- [31] D. Hazra, M. Mondal, and A. K. Gupta, “Correlation between Structural and Superconducting Properties of Nano-Granular Disordered Nb Thin Films,” *Physica C: Superconductivity*, vol. 469, no. 7–8, pp. 268–272, Apr. 2009, doi: 10.1016/j.physc.2009.02.006.
- [32] A. Rogachev and A. Bezryadin, “Superconducting Properties of Polycrystalline Nb Nanowires Tempted by Carbon Nanotubes,” *Applied Physics Letters*, vol. 83, no. 3, pp. 512–514, Jul. 2003, doi: 10.1063/1.1592313.
- [33] W. Zhou, Y. Cao, H. Zhao, Z. Li, P. Feng, and F. Feng, “Fractal Analysis on Surface Topography of Thin Films: A Review,” *Fractal and Fractional*, vol. 6, no. 3, p. 135, Feb. 2022, doi: 10.3390/fractfrac6030135.
- [34] R. Smith, “An evaluation of Fuchs-Sondheimer and Mayadas-Shatzkes models below 14nm node wide lines,” *AIP Advances*, vol. 9, no. 3, Feb. 2019, doi: 10.1063/1.5063896.
- [35] N. Pinto *et al.*, “Dimensional Crossover and Incipient Quantum Size Effects in Superconducting niobium Nanofilms,” *Scientific Reports*, vol. 8, no. 1, p. 4710, Mar. 2018, doi: 10.1038/s41598-018-22983-6.
- [36] S. A. Wolf, J. J. Kennedy, and M. Nisenoff, “Properties of superconducting rf sputtered ultrathin films of Nb,” *Journal of Vacuum Science and Technology*, vol. 13, no. 1, pp. 145–148, 1976, doi: 10.1116/1.568809.
- [37] A. V. Pronin, M. Dressel, A. Pimenov, A. Loidl, I. V. Roshchin, and L. H. Greene, “Direct observation of the superconducting energy gap developing in the conductivity spectra of niobium,” *Physical Review B*, vol. 57, no. 22, p. 14416, 1998, doi: 10.1103/PhysRevB.57.14416.
- [38] G. W. Webb, “Low-Temperature Electrical Resistivity of Pure niobium,” *Phys. Rev.*, vol. 181, no. 3, pp. 1127–1135, May 1969, doi: 10.1103/PhysRev.181.1127.
- [39] M. I. Valero-Cuadros, P. Stoliar, C. Acha, and M. Sirena, “Superconducting Properties and Electron Scattering Mechanisms in Nb-Pd thin films,” *Materials*, vol. 14, no. 23, p. 7331, 2021, doi: 10.3390/ma14237331.
- [40] D. E. Farrell *et al.*, “Resistivity and Hall effect of Nb and Ta from 1.5 to 300 K,” *Physical Review B*, vol. 52, no. 6, pp. 4473–4485, 1995, doi: 10.1103/PhysRevB.52.4473.
- [41] P. B. Allen, “Empirical electron-phonon \lambda values from resistivity of cubic metallic elements”, *Phys. Rev. B*, vol. 36, no. 5, pp. 2920–2923, Aug. 1987, doi: 10.1103/PhysRevB.36.2920.
- [42] P. B. Allen, T. P. Beaulac, F. S. Khan, W. H. Butler, F. J. Pinski, and J. C. Swihart, “dc transport in metals,” *Phys. Rev. B*, vol. 34, no. 6, pp. 4331–4333, Sep. 1986, doi: 10.1103/PhysRevB.34.4331.
- [43] S. Casalbuoni *et al.*, “Surface superconductivity in niobium for superconducting RF cavities,” *Nuclear Instruments and Methods in Physics Research Section A: Accelerators, Spectrometers, Detectors and Associated Equipment*, vol. 538, no. 1, pp. 45–64, 2005, doi: <https://doi.org/10.1016/j.nima.2004.09.003>.

- [44] A. Zeinali, T. Golod, and V. M. Krasnov, "Surface superconductivity as the primary cause of broadening of superconducting transition in Nb films at high magnetic fields," *Phys. Rev. B*, vol. 94, no. 21, p. 214506, Dec. 2016, doi: 10.1103/PhysRevB.94.214506.
- [45] K. Yoshii, H. Yamamoto, K. Saiki, and A. Koma, "Superconductivity and electrical properties in single crystalline ultrathin Nb films grown by molecular beam epitaxy," *Physical Review B*, vol. 52, pp. 13570–13575, Nov. 1995, doi: 10.1103/PhysRevB.52.13570.
- [46] F. E. Harper and M. Tinkham, "The Mixed State in Superconducting Thin Films," *Phys. Rev.*, vol. 172, no. 2, pp. 441–450, Aug. 1968, doi: 10.1103/PhysRev.172.441.
- [47] N. Pinto *et al.*, "Dimensional crossover and incipient quantum size effects in superconducting niobium nanofilms," *Scientific Reports*, vol. 8, no. 1, p. 4710, Mar. 2018, doi: 10.1038/s41598-018-22983-6.
- [48] P. R. Broussard, "Parallel Critical Field in Thin niobium Films: Comparison to Theory," *Journal of Low Temperature Physics*, vol. 189, no. 1, pp. 108–119, Oct. 2017, doi: 10.1007/s10909-017-1792-0.
- [49] S. Bose, P. Raychaudhuri, R. Banerjee, and P. Ayyub, "Upper critical field in nanostructured Nb: Competing effects of the reduction in density of states and the mean free path," *Phys. Rev. B*, vol. 74, no. 22, p. 224502, Dec. 2006, doi: 10.1103/PhysRevB.74.224502.
- [50] H. Habibullah, "30 Years of atomic force microscopy: Creep, hysteresis, cross-coupling, and vibration problems of piezoelectric tube scanners," *Measurement*, vol. 159, p. 107776, Jul. 2020, doi: 10.1016/j.measurement.2020.107776.